

Metal-Induced Energy Transfer (MIET) for Live-Cell Imaging with Fluorescent Proteins

Lara Hauke,^{||} Sebastian Isbaner,^{||} Arindam Ghosh,^{||} Isabella Guido, Laura Turco, Alexey I. Chizhik, Ingo Gregor, Narain Karedla,* Florian Rehfeldt,* and Jörg Enderlein*



Cite This: *ACS Nano* 2023, 17, 8242–8251



Read Online

ACCESS |



Metrics & More



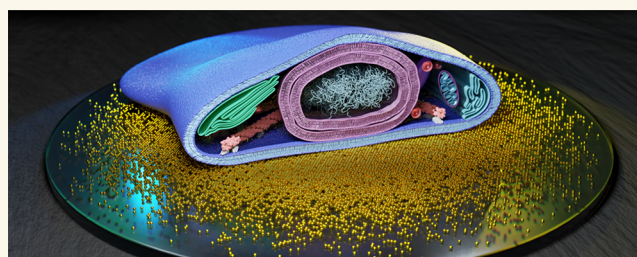
Article Recommendations



Supporting Information

ABSTRACT: Metal-induced energy transfer (MIET) imaging is an easy-to-implement super-resolution modality that achieves nanometer resolution along the optical axis of a microscope. Although its capability in numerous biological and biophysical studies has been demonstrated, its implementation for live-cell imaging with fluorescent proteins is still lacking. Here, we present its applicability and capabilities for live-cell imaging with fluorescent proteins in diverse cell types (adult human stem cells, human osteo-sarcoma cells, and *Dictyostelium discoideum* cells), and with various fluorescent proteins (GFP, mScarlet, RFP, YPet). We show that MIET imaging achieves nanometer axial mapping of living cellular and subcellular components across multiple time scales, from a few milliseconds to hours, with negligible phototoxic effects.

KEYWORDS: super-resolution microscopy, fluorescent proteins, live-cell imaging, metal-induced energy transfer, axial resolution



INTRODUCTION

Fluorescence nanoscopy¹ beyond the classical diffraction limit of optical microscopy has become an indispensable tool for modern life sciences, allowing to discern the spatial organization of biological structures down to molecular length scales. The first successful method of super-resolution microscopy was stimulated emission depletion (STED) microscopy,² which was followed by the big family of single-molecule localization microscopy (SMLM) techniques. The latter comprises photoactivated localization microscopy (PALM),³ stochastic optical reconstruction microscopy (STORM),⁴ fluorescent PALM (fPALM),⁵ direct STORM (dSTORM),⁶ and point accumulation for imaging in nanoscale topography (PAINT).⁷ These methods routinely achieve lateral resolutions down to a few dozen nanometers.

Achieving a comparable resolution along the third dimension (the optical axis) requires additional modifications of these methods: For STED, one has to apply special phase plates to generate an optical bottle along the optical axis,⁸ and for SMLM, methods such as biplane imaging,⁹ astigmatic imaging,¹⁰ wavefront shaping,¹¹ or single-molecule self-interference¹² have been developed for three-dimensional single-molecule localization. However, the axial resolution achieved by all these methods is typically by a factor of 3–5 worse than the lateral resolution, very similar to the situation encountered in classical diffraction-limited confocal microscopy.

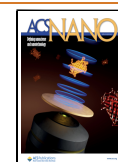
To overcome this anisotropic resolution, interferometric methods such as iPALM¹³ and isoSTED¹⁴ have been developed. These methods use two opposing objective lenses to image the sample, similar to what is done in diffraction-limited 4 π microscopy.¹⁵ While achieving truly isotropic super-resolution down to a few nanometers, these methods are technically highly complex which prevented their wide application so far. This is also true for the latest addition to the pool of super-resolution methods, MINFLUX,¹⁶ which uses a complex three-dimensional triangulation method for pinpointing the position of a single molecule with nanometric and even isotropic resolution.¹⁷

For achieving axial super-resolution close to an interface (~ 200 – 300 nm axial distance), a different family of super-resolution methods has been developed that rely on electromagnetic near-field effects. The first one is variable-angle total internal reflection fluorescence (vaTIRF) microscopy.¹⁸ It is based on conventional TIRF microscopy but records several consecutive images of the same sample under different incidence angles of the totally reflected excitation light. This

Received: December 13, 2022

Accepted: March 27, 2023

Published: March 30, 2023



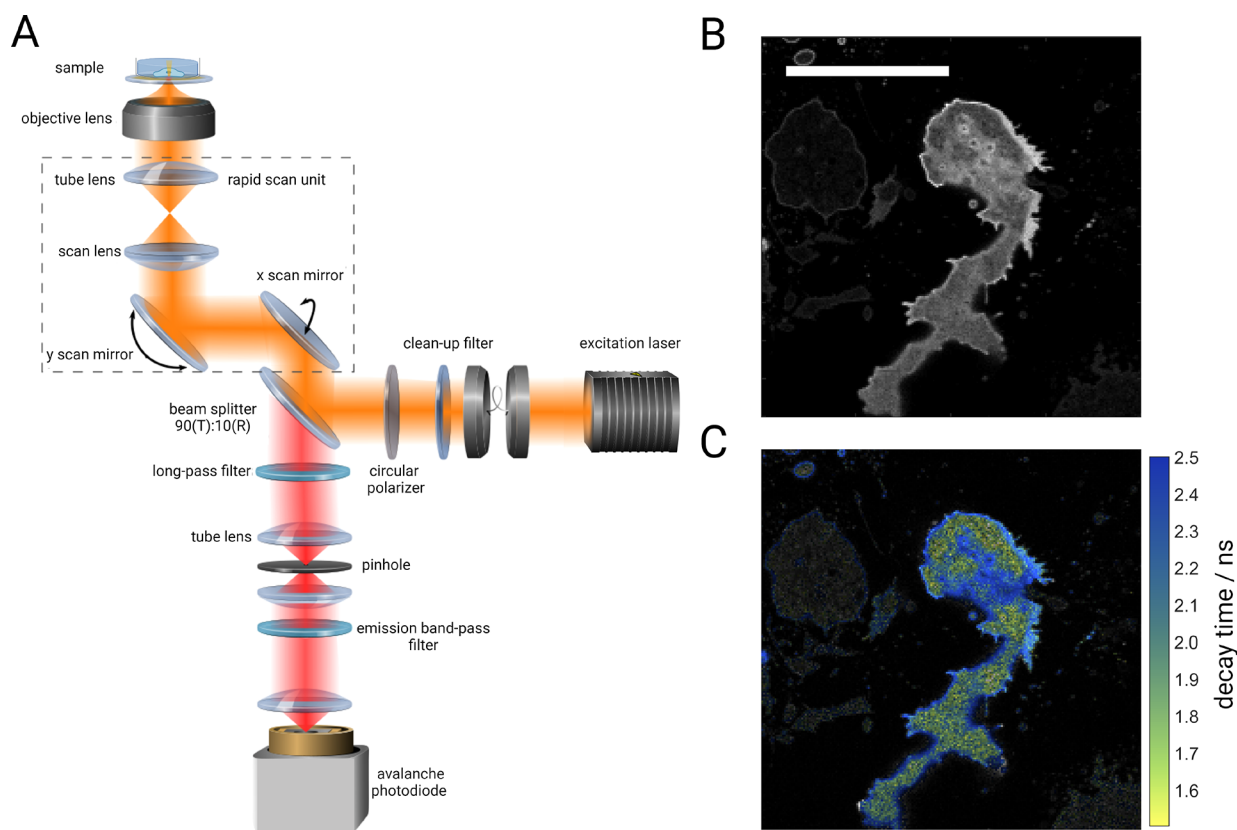


Figure 1. Experimental setup and scheme. (A) Schematic of the confocal fluorescence lifetime imaging (FLIM) microscope equipped with a rapid scanning unit (shown as dotted lines). A pulsed laser source is used for excitation. The excitation beam (shown in orange) is guided through a cleanup filter followed by a beam splitter cube (90:10) which reflects 10% of the excitation light to the scan unit. After the scan unit, the beam is focused onto the sample through a high numerical aperture objective lens. Fluorescence light is collected by the same objective and propagates through the scan unit to the beam splitter cube which transmits 90% of emission and reflects 10%. The transmitted light is then passed through an appropriate long-pass filter after which the beam is focused through a pinhole by a lens. Light after the pinhole is refocused onto the active area of a single photon-sensitive avalanche photodiode. Optionally, a band-pass filter can be used before the detector to reject residual scattering light originating from the metal film of the MIET substrate. (B and C) Intensity and fluorescence lifetime images, respectively, of an exemplary *D.d.* cell. Scale bar: 10 μm .

incidence angle variation generates evanescent excitation intensities with varying decay length. By applying an appropriate mathematical analysis, the axial distance of fluorescent structures from the glass surface can be recovered.¹⁹ The second of these near-field methods is supercritical angle fluorescence microscopy (SAF microscopy),²⁰ which uses the fact that the electromagnetic near-field of an emitting fluorescent molecule, which usually does not take part in its far-field emission (i.e., which does not contribute to observable fluorescence intensity), can couple into propagating and detectable far-field modes in the coverslip glass when the emitter comes sufficiently close to the glass surface (few hundred nanometers). These near-field-generated propagating modes travel at angles above the critical angle of total internal reflection and are thus called supercritical angle fluorescence (SAF). In contrast, the usual far-field emission of the molecule does strictly travel at angles below this critical angle (undercritical angle fluorescence or UAF). While the SAF emission intensity is strongly dependent on the distance of a molecule to the glass surface, the UAF emission intensity is independent of it. By measuring the ratio of both intensities, the axial position of an emitter can be determined with nanometer accuracy.^{21–23}

Metal-induced energy transfer (MIET) imaging exploits similar physics for achieving axial super-resolution.²⁴ Here, a

glass coverslip covered with a thin metal film is used instead. The near-field modes of the emitting fluorescent molecule, which can be modeled as an oscillating electric dipole, couple to so-called surface plasmons (collective metal electron oscillations) in the thin metal layer (typically 20 nm of gold film). This near-field coupling is similar to Förster Resonance Energy Transfer (FRET) where a fluorescent molecule (the donor) transfers its excited state energy to an acceptor molecule next to it. This energy transfer leads to a strong distance-dependent modulation of fluorescence lifetime and brightness within a distance range of 10 nm. In the case of MIET, the energy from the fluorescent molecule is transferred to metal surface plasmons, that act here as the acceptor, within a distance range similar to vaTIRF or SAF (i.e., up to ~150–200 nm).²⁵ Over this distance range, the monotonous fluorescence-lifetime–distance curve (MIET curve) can be calculated accurately using a theoretical model described thoroughly in several previous publications and which can be used to convert the measured lifetime into an emitter's axial position.^{24,25,29} Provided the availability of a fluorescence lifetime imaging microscope (FLIM), MIET does not require any modifications of the experimental setup except that it needs glass coverslips covered with a thin metal layer, which can be routinely produced today with chemical vapor deposition. For a MIET measurement, a fluorescent sample

on top of the coverslip is scanned with a focused laser beam for acquiring photons within a thin axial section with a thickness between 500 nm and 1 μm , determined by the numerical aperture of the objective and the pinhole diameter. MIET does not affect the light collection of the confocal microscope but only affects the fluorescence properties of the dyes within its range. Instead of using the brightness of a single emitter or a monolayer of emitters as in vaTIRF or SAF microscopy, MIET exploits the measured fluorescence lifetime to determine axial distances from the metal surface. This makes it more robust against intensity-affecting artifacts that may impact vaTIRF or SAF microscopy results. The localization accuracy depends on the number of detected photons which determines the accuracy of the determined fluorescence lifetime, and with a few thousand of detected photons one typically achieves an axial resolution down to a few nanometers.

Previous applications of MIET imaging include mapping the topography of the basal membrane of living cells,²⁴ three-dimensional reconstruction of focal adhesions and stress fibers,²⁶ measuring the distance between the inner and outer envelope of the nucleus,²⁷ visualizing the dynamics of epithelial–mesenchymal transitions (EMT),²⁸ single-molecule localization and colocalization,^{29,30} mapping the basal membrane and lamellipodia of human aortic endothelial cells,^{31,32} and, in combination with SMLM, three-dimensional isotropic resolution imaging of microtubules and clathrin pits.³³ Recently, it was shown that substituting the metal layer with a single sheet of graphene (graphene-induced energy transfer or GIET imaging) achieves a ca. 10-fold higher axial resolution than MIET (down to a few Ångströms), within a distance range of ~ 25 nm from the graphene.^{34–37} From here on, we refer to the axial distance of molecules or structures from the surface as height for consistency with previous works.

So far, all MIET/GIET applications mentioned above were done exclusively with synthetic organic dyes as fluorescent labels. For applying MIET to live-cell super-resolution microscopy, it is important that MIET also works with fluorescent proteins in living cells. Fluorescent proteins are widely used to label cellular structures of interest and are conveniently expressed within genetically modified living cells.³⁸ However, applying MIET to live cell imaging with fluorescent proteins is much more challenging than using MIET with synthetic organic dyes. First, one has to ensure that the average fluorescence lifetime of the used proteins is homogeneous throughout the cellular structures (in the absence of any quenching metal layer). Second, one has to cope with the usually non-monoexponential fluorescence decay of fluorescent proteins.³⁹ In the present paper, we demonstrate that fluorescent proteins (in particular, wild-type GFP and mScarlet) provide indeed fluorescent labeling with sufficiently homogeneous lifetime distributions across living cells, which is a necessary prerequisite for MIET and that the error introduced by the non-monoexponential decay of the proteins' fluorescence lifetime into the lifetime-to-distance conversion still allows for an axial resolution of approximately 10 nm. We demonstrate fluorescent-protein MIET imaging of actin stress fibers in living mammalian cells, and of the basal membrane dynamics of *Dictyostelium discoideum* (*D.d.*) cells with a nearly video-rate of imaging. Our work demonstrates the suitability of MIET for super-resolution microscopy of living cells and subcellular components labeled with fluorescent proteins while keeping phototoxicity to a minimum and achieving high temporal resolution. This is of paramount importance for the

application of MIET to a wide range of biologically important problems.

RESULTS AND DISCUSSION

Near-Video-Rate Monitoring of Changes in Cell–Substrate Adhesion of *D.d.* Cells. Fluorescence intensity and lifetime images were recorded with a home-built confocal laser-scanning microscope; see Figure 1A and the “Materials and Methods” section for details. This microscope allows for taking live-cell fluorescence lifetime images with video-rate acquisition speed (fluorescence lifetime imaging microscopy or FLIM). The first biological system that we studied were live cells of the slime mold *D.d.*, a social amoeba growing in soil and a model organism for investigating cell adhesion, motility, chemotaxis, and signal transduction.⁴⁰ Binding of cyclic AMP (cAMP) to the cells' cyclic AMP receptor 1 (cAR1) results in amplification of actin polymerization at the leading edge of *D.d.* cells, which leads to the formation of membrane protrusions known as pseudopodia.^{41,42} The cell line used in this work was derived from the axenically growing strain *D.d. carA-GFP*. MIET imaging was done for cells in their vegetative and development stages (see the “Materials and Methods” section for detailed description of cell culture and transfection protocols). Unlike mammalian cells, *D.d.* cells lack integrin. Since they can bind equally well to hydrophobic and hydrophilic surfaces, adhesion is likely governed by van der Waals interactions of membrane glycoproteins with the substrate.⁴³ Furthermore, cell–substrate adhesion changes during the developmental time of *D.d.* cells.⁴⁴ The *D.d.* cells in their developed stage used in this study were starved for 6 h and pulsed with 50 nM cAMP every 6 min over the duration of starvation. The pulsing renders the cells chemotactic, which makes them polarized and let them migrate faster toward the source of cAMP. As a result, these cells show rapid motion and membrane dynamics which makes them ideal systems for checking the live-cell imaging capabilities of MIET. Figure 1B,C shows fluorescence intensity and corresponding lifetime images of a representative *D.d.* cell where cAR1 in the cell membrane was labeled with green fluorescent protein (GFP).

We fitted recorded time-correlated single-photon counting (TCSPC) histograms from each pixel to obtain fluorescence lifetime values (see the “Materials and Methods” section for details on lifetime fitting). To convert lifetimes into heights, we first measured the (free-space) lifetime of GFP attached to cAR1 for cells on a glass slide without any metal layer. The measured value was $\tau_0 = 3.1$ ns and did not show any systematic variation across cells. Together with the fluorescence quantum yield value of GFP of $\phi = 0.79$,⁴⁵ we computed the lifetime-on-distance MIET calibration curve for cells on gold-coated glass cover slides (see the “Materials and Methods” section and Supporting Information section S3 for MIET curve calculation, Figure S7 for free-space lifetime measurement on GFP and MIET calibration curve calculation, and Figure S8 for estimated variations in height determination at various theoretical quantum yield values of GFP when attached to cAR1).

Figure 2A presents reconstructed height images obtained from FLIM images that were converted using the precalculated MIET lifetime-to-height calibration curve. Shown are cells in their developed (left panel) and vegetative stage (right panel) (see Supporting Information section S3 and Figure S9 for FLIM images and Videos S2, S2e, S3, and S3e). We observe a mean height of 47 ± 8 nm for the cell in its vegetative stage,

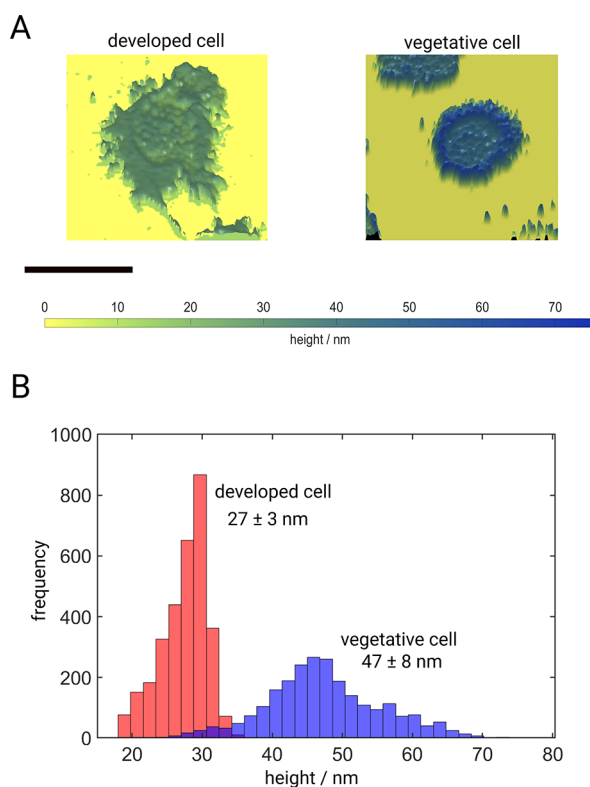


Figure 2. Live-cell MIET imaging of *D.d.* cells. (A) Images of heights of a pulsed developed cell (left) and a vegetative cell (right); see also Videos S2 and S3. Scale bar: 10 μm . (B) Histograms visualizing height profiles of the same cells as shown in panel A. The vegetative cell exhibits a mean height of 47 ± 8 nm, which is almost twice the height of the developed cell with 27 ± 3 nm.

while the cell in its developed stage approaches the surface much closer, exhibiting a mean height of 27 ± 3 nm (see Figure 2B). The much wider distribution of height values for the vegetative stage indicates significant height fluctuations for this stage. On the contrary, the developed cell pulsed with cAMP shows stronger adherence to the substrate reducing the observed temporal height fluctuations. Furthermore, we observed the formation of pseudopodia in the developed cell and its subsequent chemotactic spreading on the surface (see Video S2) which is, as expected, not observed in the vegetative cell. Another observation is that height values for the vegetative cell are nonuniform across the cell. In particular, they are higher at boundaries as compared to other areas. In contrast, the developed stage exhibits largely homogeneous height values throughout a cell. Our experiments confirm a change of the adhesion of *D.d.* cells during development as seen as a difference in height values.

FLIM images of *D.d.* cells (see Figure S9) were recorded at a frame rate of 20 Hz (see the “Materials and Methods” section). However, pertaining to the requirement of a reasonable photon budget for fluorescence lifetime fitting, further analysis was done with a $4\times$ frame binning. Figure 3A–D presents time-lapse images of a representative *D.d.* cell in its developed stage (pulsed with cAMP) over a span of 2 s at intervals of 500 ms. The false color scale indicates height values. As can be seen in the insets, our live-cell MIET imaging captures fast temporal changes in the morphology of membrane protrusions and their heights.

Three-Dimensional Architecture of Actin Stress Fibers in Mammalian Cells. The second biological system studied with FP-based live-cell MIET imaging was the three-dimensional architecture of actin stress fibers in mammalian osteosarcoma cells (SAOS-2) and in human mesenchymal stem cells (hMSCs) using electroporation with pLifeact-mScarlet (see the “Materials and Methods” section). The force transmission from contractile actomyosin stress fibers

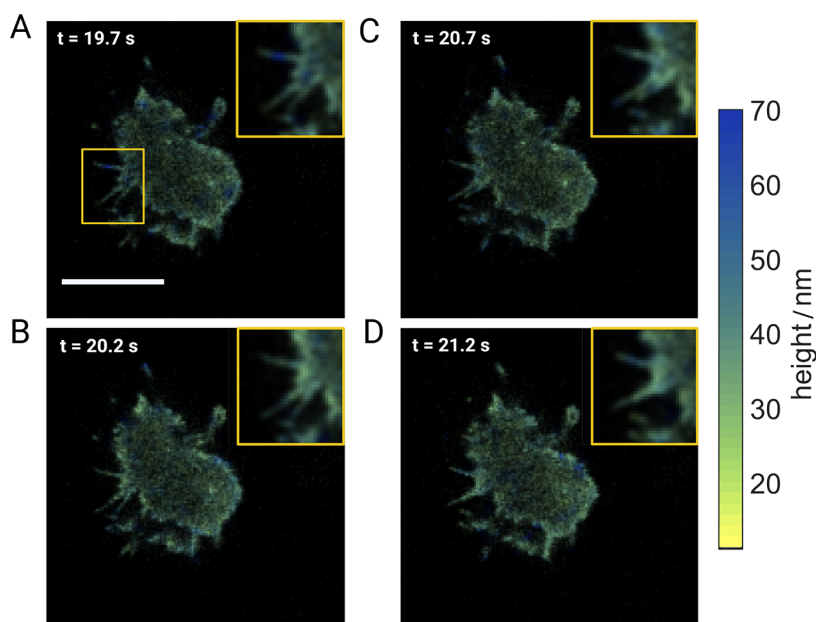


Figure 3. Live-cell MIET imaging of *D.d.* (A–D) Temporal evolution of the morphology of membrane protrusions and heights of a *D.d.* cell pulsed with cAMP at its developed stage. Original images were captured at a frame rate of 20 Hz and then binned to 5 Hz. Insets at the top right corners show magnifications of the region of interest (ROI) indicated in the first frame (top left) and detail subtle morphological changes over a time span of 1.5 s ($t = 19.7$ s to $t = 21.2$ s).

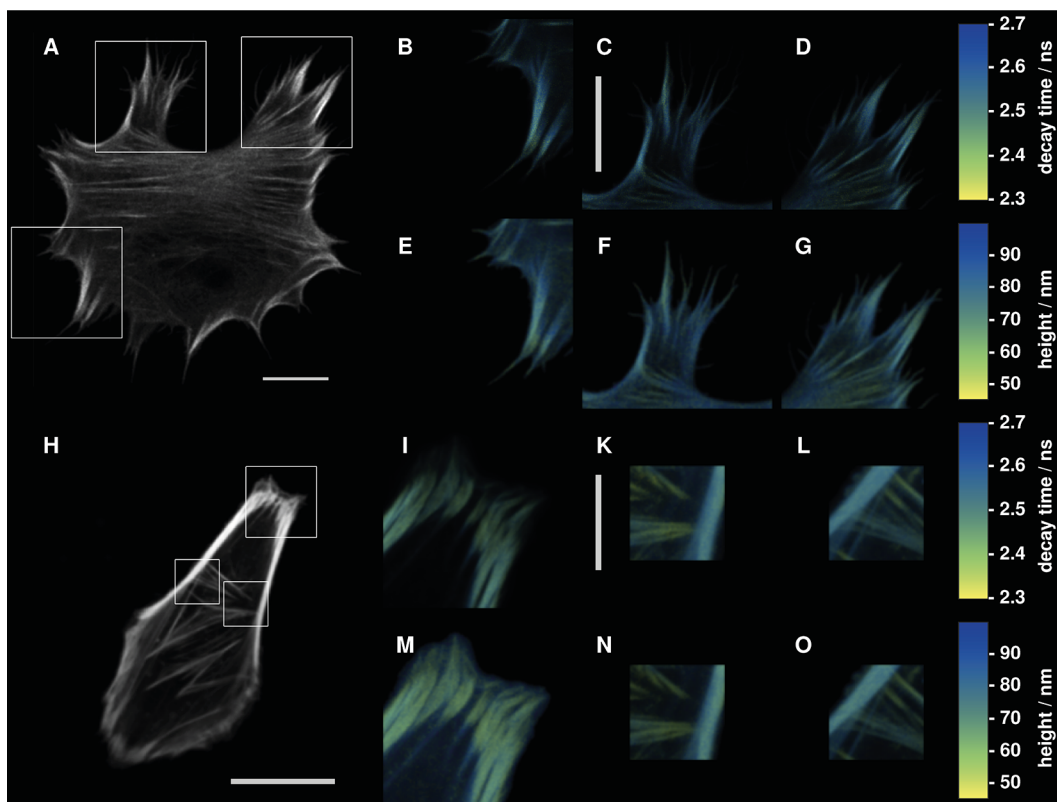


Figure 4. (A–G) hMSC cell 24 h after transfection with lifeact-mScarlet. (A) Fluorescence intensity image of the whole living cell. (B–D) Fluorescence lifetime images for different regions of interest (ROIs) indicated in panel A (white squares). (E–G) Height maps computed from the lifetime images B–D. (H–O) SAOS-2 cell 48 h after transfection with lifeact-mScarlet. (H) Fluorescence intensity image of the whole living cell. (I–L) Fluorescence lifetime images for the ROIs indicated in H. (M–O) are height maps computed from the lifetime images (I–L). All scale bars are 10 μm long.

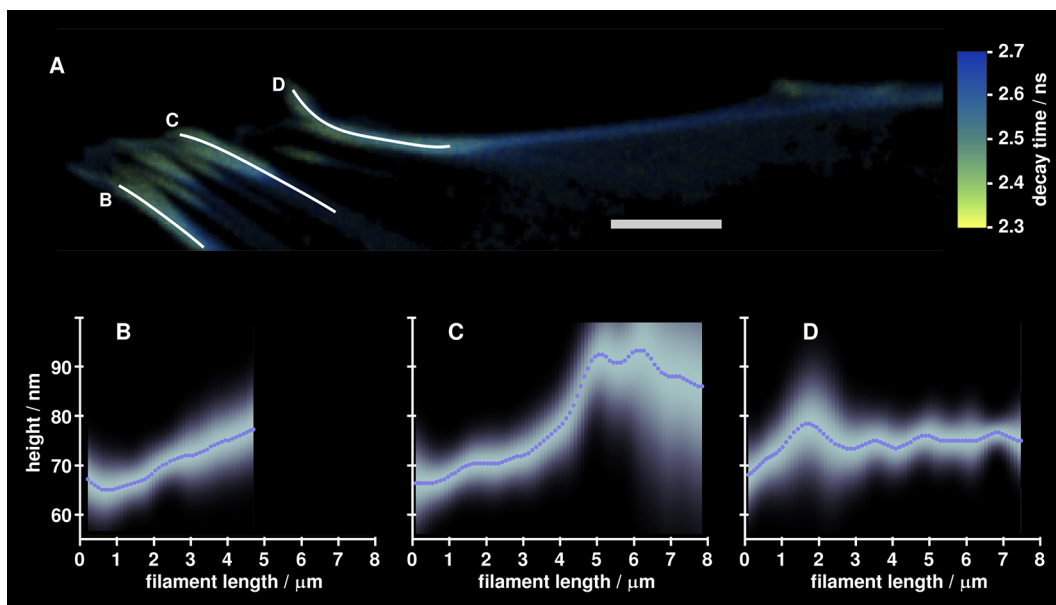


Figure 5. SAOS-2 cell 48 h after transfection with lifeact-mScarlet. (A) Fluorescence lifetime image of a cell region containing stress fibers. Three annotated fibers were chosen for further analysis. The scale bar is 5 μm . (B–D) Height curves along the three stress fibers. Dotted lines are mean values, while the density plots around these lines represent error distributions.

through focal adhesions to the cells' surroundings is a topic of intense research.⁴⁶ While much is known about structure formation and dynamics of stress fibers in two dimensions,^{47–49} the three-dimensional arrangement of proteins in

focal adhesions was resolved only recently.^{26,50} However, these studies were all done exclusively in fixed cells. For the measurements of actin fibers in life cells we tested different fluorescent proteins. Our requirements were (a) high bright-

ness in order to detect fibers near the basal membrane with short acquisition times, (b) highly monoexponential fluorescence decay, and (c) highly uniform expression levels and decay curves between different cells. Promising fluorophores with near monoexponential decay were selected based on past lifetime measurements in the lab.^{51,52} Test measurements were done with lifeact-TagRFP, -YPet, -mTurquoise, and -mScarlet (see Figures S10–S12). In our experiments, mScarlet showed the best overall performance.

We have performed MIET imaging of stress fibers in live hMSC 24 h and SAOS-2 cells 48 h after transfection. Figure 4 shows an overview of lifetime distributions for both cell lines and Figure 5 shows images of stress fibers emerging from focal adhesions together with calculated height curves. Brightness in these images corresponds to fluorescence intensity, while color encodes the fluorescence lifetime. Height profiles for the three annotated fibers in Figure 5A are shown in Figure 5B–D. This allows to reconstruct the 3D structure of stress fibers, which is important to fully understand mechanical cell–matrix interactions, in particular the direction of generated and transmitted forces. For the three analyzed stress fibers, actin heights above substrate vary from 60 to 100 nm which is in good agreement with fixed-cell measurements using interferometric PALM (iPALM)⁵⁰ and MIET imaging.⁵³ Our results show very shallow inclination angles of stress fibers with respect to the substrate surface (around 1°), which is in good agreement with our recently reported values using fixed cells and synthetic dyes.²⁶

Restructuring of the cytoskeleton and focal adhesions can occur on time scales ranging from minutes to hours. It is thus imperative to observe these cellular processes quantitatively over long periods of time. Using our MIET imaging setup, we were able to image cytoskeletal changes in living cells over 7 h; see Video S1 and the Supporting Information for details.

CONCLUSION

Our results highlight the feasibility and capabilities of MIET microscopy for axial super-resolution live-cell imaging with fluorescent proteins. We showed this for two different types of mammalian cells (hMSCs and SAOS-2) and for the slime mold *D. discoideum*, using different fluorescent proteins (mScarlet and GFP). We achieved an axial resolution of a few nanometers at an effective image rate of 5 Hz on two different developmental stages of *D. discoideum* cells, which is only limited by the brightness and density of the fluorescent proteins but not the MIET imaging microscope itself. Our results suggest that the basal membranes are twice higher from the substrate and more rugged in the vegetative stage than in the developed stage of *D. discoideum* cells. The ability to image live cells allows us to follow the temporal evolution of membrane protrusions with respect to the substrate with subsecond resolution. Furthermore, we presented long-term measurements of up to 8 h of SAOS-2 cells, demonstrating the low phototoxicity of MIET imaging, which offers the possibility to follow and quantify cellular processes with extreme axial resolution over long time scales. In particular, this will be of considerable interest for the study of the structure and dynamics of the cytoskeleton and of the focal adhesion machinery.

An important result is a demonstration that MIET imaging works well with FP labeling. FPs are on average less bright than organic dyes and do often show a non-monoexponential fluorescence lifetime decay. Nonetheless, our results show that

both these limitations still allow for decent live-cell MIET imaging with excellent signal-to-noise ratio and superior axial resolution. Considering different possible origins for the biexponential fluorescence decay we could show that we accurately estimate the radiative rate based on the average fluorescence decay time $\bar{\tau}$ (see the Supporting Information), even for nearly biexponential decays with similar amplitudes of both decay components. For typical FPs, the error of the determined height based on our calculations in Supporting Information section S1 is considerably less than 2 nm. This makes MIET imaging an ideal microscopy modality for a wide range of applications requiring live-cell imaging with fluorescent proteins. When compared to nonfluorescent interferometric techniques such as quantitative phase imaging⁵⁴ that deliver nanometer axial resolution, MIET imaging provides the specificity of fluorescence in addition to a similar axial resolution. Moreover, because MIET imaging is mostly insensitive to refractive index variations, it is not affected by inhomogeneous protein or cell organelle distributions. Taken together, we believe that live-cell MIET imaging with fluorescent proteins can be an important addition to the toolbox of axial super-resolution fluorescence microscopy techniques for cell biology.

MATERIALS AND METHODS

Cell Culture. Human mesenchymal stem cells (hMSCs) (Lonza ref. no. PT-2501, lot no. 603525) were grown in T75 cell culture flasks (Corning Inc., New York, NY, 430641U) in low glucose DMEM (Gibco, Thermo Fisher Scientific Inc., Waltham, MA, 31885–023) supplemented with 10% fetal bovine serum (Sigma-Aldrich Co., St. Louis, MO, F2442–500 ML) and 1% antibiotics (penicillin/streptomycin, Life Technologies, Thermo Fisher Scientific Inc., Waltham, MA, 15140–122) at 37 °C and 5% CO₂ and passaged every 2–3 days (cells of passage 6 were used in this study). SAOS-2 cells (DMSZ, ACC 243, RRID:CVCL_0548) were grown in T75 cell culture flasks (Sarstedt, Nümbrecht, Germany, 833.911.002) in McCoy's 5A (Gibco, Thermo Fisher Scientific Inc., Waltham, MA, 26600–23) supplemented with 15% fetal bovine serum (Sigma-Aldrich Co., St. Louis, MO, F2442–500 ML) and 1% antibiotics (penicillin/streptomycin, Life Technologies, Thermo Fisher Scientific Inc., Waltham, MA, 15140–122) at 37 °C and 5% CO₂ and passaged every 4 days (passage 13 was used in these experiments). CarA-GFP *D.d.* cells were cultivated in HLS medium (Formedium) at 22 °C on polystyrene Petri dishes (Primaria, Falcon, BD Becton Dickinson) and passaged every 2–3 days. As long as nutrients are available (HLS medium), *D.d.* cells proliferate as unicellular amoeba and are defined as vegetative cells. When the cells deplete their food source and start to starve (in our case, the HLS medium is removed and replaced by buffer), they enter a developmental cycle. For the preparation of experiments, cells were starved in shaking phosphate buffer at 150 rpm (PB, 2 g of KH₂PO₄ and 0.36 g of Na₂HPO₄·2H₂O per 1 L, pH 6) for 5 h at a density of 2×10^6 cells/mL. The shaking culture was pulsed with 50 nM cAMP (Sigma) every 6 min over the course of the starvation time. After the corresponding starvation time, the cells were harvested and washed in PB. An aliquot of the cell suspension was applied to the experimental setup and the cells were allowed to spread on the glass substrate for 10 min at room temperature before starting the experiment. For experiments with vegetative *D.d.* cells, they were detached from the Petri dish bottom, washed twice with PB, and applied directly to the experimental setup without any additional starvation time.

Transfection. Cells were transfected with the plasmid pLifeAct_mScarlet-i_N1, a gift from Dorus Gadella (Addgene plasmid #85056, RRID:Addgene_85056), using the Lonza 4D Nucleofector (Lonza, Cologne, Germany, AAF-1002B & AAF-1002X). hMSCs were transfected using the P1 buffer (Lonza, Cologne, Ger, V4XP-1012) and pulse code FF-104. SAOS-2 cells were transfected using

the SF buffer (Lonza, Cologne, Ger, V4XC-2012) and pulse code DS-150. Subsequent to transfection cells were seeded onto prepared dishes at 80,000 cells per well. Dead cells were removed by rinsing with medium 12 h after transfection. The cell line carA-GFP were derived from the axenically growing strain *D.d.* AX3. They were kindly provided by G. Gerisch (Max Planck Institute for Biochemistry, Martinsried, Germany).

Sample Preparation. For SAOS-2 and hMSC measurements, glass coverslips of 25 mm diameter (VWR, Darmstadt, Ger, ECN631–1584) were covered with 2 nm of Ti, 15 nm of Au, 1 nm of Ti, 20 nm of SiO₂. Both, gold-coated and regular glass coverslips were cleaned and functionalized with collagen-I using heterobifunctional cross-linking chemistry as described earlier.⁵⁵ In brief, all slides were plasma cleaned for 15 min, sonicated first using 99% EtOH and second using 2% APTES (Sigma-Aldrich Co., St. Louis, MO, 440140) in EtOH and treated with a 0.5% glutaraldehyde solution (Sigma-Aldrich Co., St. Louis, MO, C7651). Glasses were rinsed twice with PBS and once with HEPES buffer. Sulfo-SANPAH (Thermo Fisher Scientific Inc., Waltham, MA, 22589) was added to the surface and activated under UV for 10 min. A solution of 0.2 mg/mL collagen I (Rat tail collagen I, Corning Inc., New York, NY, 354236) in PBS is added and incubated overnight at 4 °C. Glasses are rinsed twice with PBS and glued into bottomless ibidi dishes (ibidi, Gräfeling, Ger, DIO01110) using UV-curable glue (NOA68, Norland products inc., Cranbury, NJ, 6801). Prepared dishes are UV sterilized for 2 h and rinsed three times with PBS before seeding of cells. For MIET measurements on *D.d.* cells, glass coverslips were first sonicated with 1 M KOH and plasma cleaned for 15 min. These cleaned coverslips were then coated with a 2 nm titanium layer (for better sticking of gold on glass) followed by evaporation of 15 nm of gold, 1 nm of titanium, and 10 nm of SiO₂. Gold-coated coverslips were then glued into bottomless ibidi dishes (ibidi, Gräfeling, Ger, DIO01110) using UV-curable glue (NOA68, Norland Products Inc., Cranbury, NJ, 6801). Prepared dishes are UV sterilized for 2 h and rinsed three times with PBS before seeding of cells.

Imaging. Cells were imaged in phenol-red-free DMEM (Gibco, Thermo Fisher Scientific Inc., Waltham, MA, 11880–028) supplemented with 12.5% fetal bovine serum (Sigma-Aldrich Co., St. Louis, MO, F2442–500 ML) and 1% antibiotics (penicillin/streptomycin, Life Technologies, Thermo Fisher Scientific Inc., Waltham, MA, 15140-122) at 37 °C, 5% CO₂, and 80% humidity using a climatic chamber (ibidi, Gräfeling, Ger, 10918) and gas mixer with humidifier column (ibidi, Gräfeling, Germany, #11922-DS). CarA-GFP *D.d.* cells were imaged in PB at room temperature.

Setup. Fluorescence lifetime images were acquired on a custom-built confocal setup. The excitation light was generated by an 80 MHz pulsed white-light laser (SuperK Power, Koheras) and the wavelength was selected by an AOTF (SpectraK Dual, Koheras). The beam was coupled into a single-mode fiber (PMC-460Si-3,0-NA012-3APC-150-P and fiber coupler 60SMS-1-4-RGBV-11–47, both Schäfer+Kirchhoff GmbH, Germany) and after the fiber recollimated by an objective (UPlanSApo 10×, 0.40 N.A., Olympus). After passing a cleanup filter (F37–563 and F49–488 (for *D.d.* measurements), AHF), a 90/10 beam splitter was used to reflect the excitation light into the microscope and separate it from the emission. The reflected beam was directed into a laser scanning system (FLIMbee, PicoQuant) and then into a custom side port of the microscope (Olympus IX73). The three galvo mirrors in the scanning system are imaged onto the backfocal plane of the objective (UApo N, 100×, 1.49 N.A. oil, Olympus) with 180 mm and 90 mm achromatic lenses. The sample could be moved by a manual xy-stage (Olympus) and a z-piezo stage (Nano-ZL100, MadCityLabs). Fluorescence in the sample was collected by the same objective and descanned in the scanning system. The fluorescence light that passed the 90/10 beam splitter was then focused onto a pinhole (100 μm, Thorlabs) with a 180 mm achromatic lens. Backscattered laser light was blocked by a long-pass filter (S68 LP Edge Basic, Semrock and F76–490 for *D.d.* GFP measurements). The light was collimated by a 100 mm lens and passed through a bandpass filter (FF01–593/40–25, AHF and F37–521 525/45, AHF for *D.d.* GFP measurements) before a lens (*f* = 30 mm, Thorlabs) focused the

light onto the detector (*τ*-SPAD, PicoQuant). The signal of the photon detector was recorded by a TCSPC system (HydraHarp 400, PicoQuant) together with the trigger signal by the laser. FLIM images were recorded with the SymPhoTime 64 software (PicoQuant) which controlled the TCSPC system and the laser scanner. Typically, a pixel size of 100 nm was chosen with a pixel dwell time of 20 μs and a TCSPC resolution of 16 ps. For *D.d.* GFP measurements, a pixel size of 150 nm was chosen with a pixel dwell time of 2 μs and a TCSPC resolution of 16 ps. To monitor the axial focus position, back-reflected light was coupled out from the excitation beam with an additional 90/10 beam splitter and focused (*f* = 200 mm, Thorlabs) onto a camera (Guppy GF036B ASG, Allied Vision Technologies).

Data Analysis. Data analysis was carried out using custom routines written in Matlab (MathWorks). First, scan lines were aligned using a linear shift. Then, TCSPC histograms of individual pixels were generated and corrected for dead-time artifacts.⁵⁶ A monoexponential fit including a measured instrument response function (IRF) was used to estimate the fluorescence lifetime. The TCSPC curve was fitted with the function

$$f(t|\tau, a, b, s, a_s) = b + \int dt' \left[\chi(t - t' - s) \frac{a}{\tau} \exp\left(-\frac{t'}{\tau}\right) + a_s \chi(t - s) \right] \quad (1)$$

where $\chi(t)$ denotes the instrumental response function of the TCSPC system, τ denotes the fluorescence lifetime, a denotes the fit amplitude, b denotes the background, a_s denotes the scattering amplitude, and s denotes the color shift of the IRF. The scattering amplitude accounts for the luminescence of the gold, and the shift s was introduced as the IRF depends on the count rate. We found for our detectors that linear shifts was sufficient to account for this effect. The lifetime was converted into a height using the appropriate MIET curve for the sample. Images and movies were created with the lifetime or height information in color, using the intensity (rescaled to 0–1) as the transparency of the image.

MIET Curve Calculation. The theoretical curve for converting measured lifetimes into heights were computed based on the model by Chance, Prock, and Silbey.^{25,57,58} For the substrate, we assumed a layered system of (from bottom to top): glass, 2 nm of titanium, 15 nm of gold, 1 nm of titanium, and 20 nm of silica. The medium of the fluorophores and above was assumed to have the refractive index of water, refractive indices of the metals were taken from literature.⁵⁹ The theoretical MIET curve for GFP in connection to *D.d.* measurements were calculated similarly where we assumed a layered system (from bottom to top) glass, 2 nm of titanium, 15 nm of gold, 1 nm of titanium, and 10 nm of silica. Please see [Supporting Information section S3](#) for the theoretical MIET curve.

Impact of Multiexponential Fluorescence Decays. Like other methods that take advantage of fluorescence quenching (Förster resonance energy transfer, Stern–Volmer quenching) the analysis is based on the fluorescence decay time, being the inverse of the rates depopulating the excited state. These are the emission rate k_{fl} and nonradiative processes that are summarized into k_{nr} . The quenching adds a further rate to the total and the analysis is all about quantifying this additional contribution. For this, k_{fl} and k_{nr} are assumed to be constant and can be obtained from the fluorescence decay time and the quantum yield of the dye in “free-space” conditions. All these processes lead to a strictly monoexponential decay of the decay allowing seamless analysis of the data. In reality, however, one usually observes fluorescence decays that deviate from the expected behavior. Most common are biexponential decays. These are usually explained as two populations of slightly different forms of the fluorophore (e.g., in a different local environment, charges near the chromophoric part of the molecule etc.).

Accurate determination of two lifetimes and their respective contribution to the decay is surprisingly hard and requires collecting many photons. Therefore, we estimate the amount of quenching based on the average fluorescence decay time, which can be

determined quite simply and reliably. For checking how this simplified analysis impacts the obtained height values, we simulated biexponential decays based on the rate constants of lifeact-mScarlet and the MIET curve (applied to each monoexponential decay component). The average lifetime of these decays was determined and used to calculate a height values using again the MIET curve. The results prove that the analysis based on the average fluorescence decay time adds no significant error to the determined height values of the fluorophores (see [Supporting Information section S1](#)).

Protein Expressions for Quantum Yield Measurement. *lifeact-mScarlet* from SAOS-2. For quantum yield measurements, SAOS-2 cells (passage 13) were cultured and transfected as previously mentioned. The fusion protein (*lifeact-mScarlet*) was extracted using a RFP-Trap (Chromotek, Planegg–Martinsried, Germany, rta-20). Cells were harvested, lysed, and protein was extracted as advised by vendor. For elution, we bound proteins by adding 50 μ L of 0.2 M glycine (pH 2.5) under 30 s of constant mixing. After 2 min of centrifugation at 2.500 g, the supernatant was transferred to a new tube and pH neutralized by the addition of 5 μ L of 1 M Tris base (pH 10.4).

lifeact-mScarlet-6His in *E. coli*. The *lifeact-mScarlet* sequence was cut out using NdeI and XhoI sites and inserted into pET24b+ vector (Sigma-Aldrich Co., St. Louis, MO, 39750), yielding a 6-His Tag on the mScarlet. Construct was electroporated into *E. coli* (BL21-Gold Competent Cells) (Agilent Technologies, Santa Clara, CA, #230130) and plated on LB plates (Sigma-Aldrich Co., St. Louis, MO, S2062) with kanamycin (Sigma-Aldrich Co., St. Louis, MO, 70560–51–9). Growing cultures were sequenced (Sanger Sequencing, Microsynth Seqlab, Göttingen, Ger) and expressed in 500 mL of LB Medium (Sigma-Aldrich Co., St. Louis, MO, S1208) for 5 h before harvesting. Cultures were spun down, and the pellets subjected to lysis buffer (50 mM Tris/Cl pH 8.0, 250 mM NaCl, 10 mM β -mercaptoethanol, 1 mM PMSF). *lifeact-mScarlet-6His* was bound to Protino NiNTA agarose (Macherey-Nagel, Düren, Ger, 745400.25) and washed (50 mM Tris/Cl pH 8.0, 250 mM NaCl, 10 mM β -Mercaptoethanol, 20 mM Imidazol). NiNTA beads were given into a empty Protino column (Macherey-Nagel, Düren, Ger, 745400.10) and washed again. A final elution was done 5 times with 1 mL of elution buffer (50 mM Tris/Cl pH 8.0, 250 mM NaCl, 10 mM β -mercaptoethanol, 250 mM imidazol) for 30 min each, and samples were frozen at -80 °C. Samples were checked with a SDS-PAGE gel.

ASSOCIATED CONTENT

Supporting Information

The Supporting Information is available free of charge at <https://pubs.acs.org/doi/10.1021/acsnano.2c12372>.

Details about height determination of molecule's from their average lifetime; GFP and mScarlet lifetime measurements and MIET calibration curves; additional TCSPC data for various fluorescent proteins ([PDF](#))

Video S1: part of a migrating SAOS-2 cell at 96 hours post-transfection with *lifeact-mScarlet* ([AVI](#))

Videos S2 and S2e: proliferation and membrane dynamics of developed *D.d.* cells pulsed with cAMP; Video S2 corresponds to [Figure 2](#) displayed in the main text, and Video S2e illustrates the error values in height determination per pixel of Video S2 ([AVI](#), [AVI](#))

Videos S3 and S3e: dynamics of *D.d.* cells in their vegetative stage; Video S3 corresponds to [Figure 2](#) displayed in the main text, and Video S3e illustrates the error values in height determination per pixel of Video S3 ([AVI](#), [AVI](#))

AUTHOR INFORMATION

Corresponding Authors

Narain Karedla – Third Institute of Physics – Biophysics, Georg August University, 37077 Göttingen, Germany; Present Address: N.K.: Kennedy Institute of Rheumatology, University of Oxford, Oxford OX3 7LF, United Kingdom; Email: narain.karedla@kennedy.ox.ac.uk

Florian Rehfeldt – Third Institute of Physics – Biophysics, Georg August University, 37077 Göttingen, Germany; Present Address: F.R.: Experimental Physics I, University of Bayreuth, Universitätsstrasse 30, 95440 Bayreuth, Germany; Email: florian.rehfeldt@uni-bayreuth.de

Jörg Enderlein – Third Institute of Physics – Biophysics, Georg August University, 37077 Göttingen, Germany; Cluster of Excellence “Multiscale Bioimaging: from Molecular Machines to Networks of Excitable Cells” (MBExC), Universitätsmedizin Göttingen, 37075 Göttingen, Germany; orcid.org/0000-0001-5091-7157; Email: jenderl@gwdg.de

Authors

Lara Hauke – Third Institute of Physics – Biophysics, Georg August University, 37077 Göttingen, Germany; Present Address: L.H.: Institute of Pharmacology and Toxicology, University Medical Center Göttingen, Robert-Koch-Strasse 40, 37075 Göttingen, Germany

Sebastian Isbaner – Third Institute of Physics – Biophysics, Georg August University, 37077 Göttingen, Germany; orcid.org/0000-0001-6582-0673

Arindam Ghosh – Third Institute of Physics – Biophysics, Georg August University, 37077 Göttingen, Germany; Present Address: A.G.: Department of Biotechnology and Biophysics, Biocenter, University of Würzburg, Am Hubland, 97074 Würzburg, Germany; orcid.org/0000-0002-5712-1271

Isabella Guido – Max Planck Institute for Dynamics and Self-Organization, 37077 Göttingen, Germany; orcid.org/0000-0002-1781-3767

Laura Turco – Max Planck Institute for Dynamics and Self-Organization, 37077 Göttingen, Germany

Alexey I. Chizhik – Third Institute of Physics – Biophysics, Georg August University, 37077 Göttingen, Germany

Ingo Gregor – Third Institute of Physics – Biophysics, Georg August University, 37077 Göttingen, Germany; orcid.org/0000-0002-1775-2159

Complete contact information is available at: <https://pubs.acs.org/doi/10.1021/acsnano.2c12372>

Author Contributions

^{||}L.H., S.I., and A.G. contributed equally to this work.

Notes

The work has previously been made available as a preprint: Hauke, L.; Isbaner, S.; Ghosh, A.; Guido, I.; Turco, L.; Chizhik, A. I.; Gregor, I.; Karedla, N.; Rehfeldt, F.; Enderlein, J. Metal-Induced Energy Transfer (MIET) for Live-Cell Imaging with Fluorescent Proteins. *bioRxiv*(Biophysics), November 13, 2022, 516247, DOI: [10.1101/2022.11.12.516247](https://doi.org/10.1101/2022.11.12.516247).

The authors declare no competing financial interest.

ACKNOWLEDGMENTS

This work was financially supported by the Deutsche Forschungsgemeinschaft (DFG, German Research Foundation) via project B08 (L.H. and F.R.) of the Collaborative Research Center 755 (SFB 755) and project A13 (L.H. and F.R.) of the Collaborative Research Center 937 (SFB 937). A.G. and J.E. thank the Deutsche Forschungsgemeinschaft (SFB 860, project A06, DFG, German Research Foundation). J.E. acknowledges financial support by the DFG through Germany's Excellence Strategy EXC 2067/1-390729940. J.E. thanks the European Research Council (ERC) for financial support via project "smMIET" (grant agreement no. 884488) under the European Union's Horizon 2020 research and innovation program.

REFERENCES

- (1) Hell, S. W. Far-field optical nanoscopy. *Science* **2007**, *316*, 1153–1158.
- (2) Hell, S. W.; Wichmann, J. Breaking the diffraction resolution limit by stimulated emission: stimulated-emission-depletion fluorescence microscopy. *Opt. Lett.* **1994**, *19*, 780–782.
- (3) Betzig, E.; Patterson, G. H.; Sougrat, R.; Lindwasser, O. W.; Olenych, S.; Bonifacino, J. S.; Davidson, M. W.; Lippincott-Schwartz, J.; Hess, H. F. Imaging intracellular fluorescent proteins at nanometer resolution. *Science* **2006**, *313*, 1642–1645.
- (4) Rust, M. J.; Bates, M.; Zhuang, X. Sub-diffraction-limit imaging by stochastic optical reconstruction microscopy (STORM). *Nat. Methods* **2006**, *3*, 793.
- (5) Hess, S. T.; Girirajan, T. P.; Mason, M. D. Ultra-high resolution imaging by fluorescence photoactivation localization microscopy. *Biophys. J.* **2006**, *91*, 4258–4272.
- (6) Heilemann, M.; Van De Linde, S.; Schüttelpelz, M.; Kasper, R.; Seefeldt, B.; Mukherjee, A.; Tinnefeld, P.; Sauer, M. Subdiffraction-resolution fluorescence imaging with conventional fluorescent probes. *Angew. Chem., Int. Ed.* **2008**, *47*, 6172–6176.
- (7) Sharonov, A.; Hochstrasser, R. M. Wide-field subdiffraction imaging by accumulated binding of diffusing probes. *Proc. Natl. Acad. Sci. U. S. A.* **2006**, *103*, 18911–18916.
- (8) Wildanger, D.; Medda, R.; Kastrup, L.; Hell, S. A compact STED microscope providing 3D nanoscale resolution. *J. Microsc.* **2009**, *236*, 35–43.
- (9) Jüette, M. F.; Gould, T. J.; Lessard, M. D.; Mlodzikowski, M. J.; Nagpure, B. S.; Bennett, B. T.; Hess, S. T.; Bewersdorff, J. Three-dimensional sub-100 nm resolution fluorescence microscopy of thick samples. *Nat. Methods* **2008**, *5*, 527–529.
- (10) Huang, B.; Wang, W.; Bates, M.; Zhuang, X. Three-dimensional super-resolution imaging by stochastic optical reconstruction microscopy. *Science* **2008**, *319*, 810–813.
- (11) Backlund, M. P.; Lew, M. D.; Backer, A. S.; Sahl, S. J.; Grover, G.; Agrawal, A.; Piestun, R.; Moerner, W. Simultaneous, accurate measurement of the 3D position and orientation of single molecules. *Proc. Natl. Acad. Sci. U. S. A.* **2012**, *109*, 19087–19092.
- (12) Bon, P.; Linarès-Loyez, J.; Feyeux, M.; Alessandri, K.; Lounis, B.; Nassoy, P.; Cognet, L. Self-interference 3D super-resolution microscopy for deep tissue investigations. *Nat. Methods* **2018**, *15*, 449–454.
- (13) Shtengel, G.; Galbraith, J. A.; Galbraith, C. G.; Lippincott-Schwartz, J.; Gillette, J. M.; Manley, S.; Sougrat, R.; Waterman, C. M.; Kanchanawong, P.; Davidson, M. W.; et al. Interferometric fluorescent super-resolution microscopy resolves 3D cellular ultrastructure. *Proc. Natl. Acad. Sci. U. S. A.* **2009**, *106*, 3125–3130.
- (14) Aquino, D.; Schönlé, A.; Geisler, C.; Middendorff, C. v.; Wurm, C. A.; Okamura, Y.; Lang, T.; Hell, S. W.; Egner, A. Two-color nanoscopy of three-dimensional volumes by 4Pi detection of stochastically switched fluorophores. *Nat. Methods* **2011**, *8*, 353–359.
- (15) Hell, S.; Stelzer, E. H. Properties of a 4Pi confocal fluorescence microscope. *Journal of the Optical Society of America A* **1992**, *9*, 2159–2166.
- (16) Balzarotti, F.; Eilers, Y.; Gwosch, K. C.; Gynnå, A. H.; Westphal, V.; Stefani, F. D.; Elf, J.; Hell, S. W. Nanometer resolution imaging and tracking of fluorescent molecules with minimal photon fluxes. *Science* **2017**, *355*, 606–612.
- (17) Gwosch, K. C.; Pape, J. K.; Balzarotti, F.; Hoess, P.; Ellenberg, J.; Ries, J.; Hell, S. W. MINFLUX nanoscopy delivers 3D multicolor nanometer resolution in cells. *Nat. Methods* **2020**, *17*, 217–224.
- (18) Stock, K.; Sailer, R.; Strauss, W. S.; Lyttke, M.; Steiner, R.; Schneckenburger, H. Variable-angle total internal reflection fluorescence microscopy (VA-TIRFM): realization and application of a compact illumination device. *J. Microsc.* **2003**, *211*, 19–29.
- (19) El Arawi, D.; Vézy, C.; Déturche, R.; Lehmann, M.; Kessler, H.; Döntenwill, M.; Jaffiol, R. Advanced quantification for single-cell adhesion by variable-angle TIRF nanoscopy. *Biophysical Reports* **2021**, *1*, 100021.
- (20) Ruckstuhl, T.; Verdes, D. Supercritical angle fluorescence (SAF) microscopy. *Opt. Express* **2004**, *12*, 4246–4254.
- (21) Winterlood, C. M.; Ruckstuhl, T.; Verdes, D.; Seeger, S. Nanometer axial resolution by three-dimensional supercritical angle fluorescence microscopy. *Phys. Rev. Lett.* **2010**, *105*, 108103.
- (22) Deschamps, J.; Mund, M.; Ries, J. 3D superresolution microscopy by supercritical angle detection. *Opt. Express* **2014**, *22*, 29081–29091.
- (23) Jouchet, P.; Cabriel, C.; Bourg, N.; Bardou, M.; Poüs, C.; Fort, E.; Lévêque-Fort, S. Nanometric axial localization of single fluorescent molecules with modulated excitation. *Nat. Photonics* **2021**, *15*, 297–304.
- (24) Chizhik, A. I.; Rother, J.; Gregor, I.; Janshoff, A.; Enderlein, J. Metal-Induced Energy Transfer for live cell nanoscopy. *Nat. Photonics* **2014**, *8*, 124.
- (25) Enderlein, J. Single-molecule fluorescence near a metal layer. *Chem. Phys.* **1999**, *247*, 1–9.
- (26) Chizhik, A. M.; Wollnik, C.; Ruhlandt, D.; Karedla, N.; Chizhik, A. I.; Hauke, L.; Hähnel, D.; Gregor, I.; Enderlein, J.; Rehfeldt, F. Dual-color Metal-Induced and Förster Resonance Energy Transfer for cell nanoscopy. *Molecular Biology Of The Cell* **2018**, *29*, 846–851.
- (27) Chizhik, A. M.; Ruhlandt, D.; Pfaff, J.; Karedla, N.; Chizhik, A. I.; Gregor, I.; Kehlenbach, R. H.; Enderlein, J. Three-dimensional reconstruction of nuclear envelope architecture using dual-color Metal-Induced Energy Transfer Imaging. *ACS Nano* **2017**, *11*, 11839–11846.
- (28) Baronsky, T.; Ruhlandt, D.; Brückner, B. R.; Schäfer, J.; Karedla, N.; Isbaner, S.; Hähnel, D.; Gregor, I.; Enderlein, J.; Janshoff, A.; et al. Cell-substrate dynamics of the epithelial-to-mesenchymal transition. *Nano Lett.* **2017**, *17*, 3320–3326.
- (29) Karedla, N.; Chizhik, A. I.; Gregor, I.; Chizhik, A. M.; Schulz, O.; Enderlein, J. Single-molecule Metal-Induced Energy Transfer (smMIET): Resolving nanometer distances at the single-molecule level. *ChemPhysChem* **2014**, *15*, 705–711.
- (30) Isbaner, S.; Karedla, N.; Kaminska, I.; Ruhlandt, D.; Raab, M.; Bohlen, J.; Chizhik, A.; Gregor, I.; Tinnefeld, P.; Enderlein, J.; et al. Axial Colocalization of Single Molecules with Nanometer Accuracy Using Metal-Induced Energy Transfer. *Nano Lett.* **2018**, *18*, 2616–2622.
- (31) Hwang, W.; Seo, J.; Kim, D.; Lee, C. J.; Choi, I.-H.; Yoo, K.-H.; Kim, D. Y. Large field-of-view nanometer-sectioning microscopy by using metal-induced energy transfer and biexponential lifetime analysis. *Commun. Biol.* **2021**, *4*, 91.
- (32) Hwang, W.; Kim, D.; Kim, D. Axial scanning Metal-Induced Energy Transfer Microscopy for extended range nanometer-sectioning cell imaging. *Small* **2022**, *18*, 2105497.
- (33) Thiele, J. C.; Jungblut, M.; Helmerich, D. A.; Tsukanov, R.; Chizhik, A.; Chizhik, A. I.; Schnermann, M. J.; Sauer, M.; Nevskiy, O.; Enderlein, J. Isotropic three-dimensional dual-color super-resolution microscopy with metal-induced energy transfer. *Science Advances* **2022**, *8*, No. eabo2506.

- (34) Ghosh, A.; Sharma, A.; Chizhik, A. I.; Isbaner, S.; Ruhlandt, D.; Tsukanov, R.; Gregor, I.; Karedla, N.; Enderlein, J. Graphene-based metal-induced energy transfer for sub-nanometre optical localization. *Nat. Photonics* **2019**, *13*, 860–865.
- (35) Ghosh, A.; Chizhik, A. I.; Karedla, N.; Enderlein, J. Graphene and metal-induced energy transfer for single-molecule imaging and live-cell nanoscopy with (sub)-nanometer axial resolution. *Nat. Protoc.* **2021**, *16*, 3695–3715.
- (36) Füllbrunn, N.; Li, Z.; Jorde, L.; Richter, C. P.; Kurre, R.; Langemeyer, L.; Yu, C.; Meyer, C.; Enderlein, J.; Ungermann, C.; et al. Nanoscopic anatomy of dynamic multi-protein complexes at membranes resolved by graphene-induced energy transfer. *eLife* **2021**, *10*, No. e62501.
- (37) Raja, S. O.; Chizhik, A. I.; Schmidt, C. F.; Enderlein, J.; Ghosh, A. Mapping activity-dependent quasi-stationary states of mitochondrial membranes with Graphene-Induced Energy Transfer imaging. *Nano Lett.* **2021**, *21*, 8244–8249.
- (38) Wiedenmann, J.; Oswald, F.; Nienhaus, G. U. Fluorescent proteins for live cell imaging: Opportunities, limitations, and challenges. *IUBMB Life* **2009**, *61*, 1029–1042.
- (39) Ghosh, A.; Isbaner, I.; Veiga-Gutierrez, M.; Gregor, I.; Enderlein, J.; Karedla, N. Quantifying microsecond transition times using fluorescence lifetime correlation spectroscopy. *J. Phys. Chem. Lett.* **2017**, *8*, 6022–6028.
- (40) Loomis, W. *Dictyostelium Discoideum: A Developmental System*; Academic Press: New York, 1975.
- (41) Singer, G.; Araki, T.; Weijer, C. J. Oscillatory cAMP cell-cell signalling persists during multicellular Dictyostelium development. *Commun. Biol.* **2019**, *2*, 139.
- (42) Varnum-Finney, B. J.; Voss, E.; Soll, D. R. Frequency and orientation of pseudopod formation of Dictyostelium discoideum amoebae chemotaxing in a spatial gradient: further evidence for a temporal mechanism. *Cell Motil. Cytoskeleton* **1987**, *8*, 18–26.
- (43) Loomis, W. F. Genetic control of morphogenesis in Dictyostelium. *Dev. Biol.* **2015**, *402*, 146–161.
- (44) Tarantola, M.; Bae, A.; Fuller, D.; Bodenschatz, E.; Rappel, W.-J.; Loomis, W. F. Cell substratum adhesion during early development of Dictyostelium discoideum. *PLoS One* **2014**, *9*, e106574.
- (45) Patterson, G. H.; Knobel, S. M.; Sharif, W. D.; Kain, S. R.; Piston, D. W. Use of the green fluorescent protein and its mutants in quantitative fluorescence microscopy. *Biophys. J.* **1997**, *73*, 2782–2790.
- (46) Paluch, E. K.; Nelson, C. M.; Biais, N.; Fabry, B.; Moeller, J.; Pruitt, B. L.; Wollnik, C.; Kudryasheva, G.; Rehfeldt, F.; Federle, W. Mechanotransduction: use the force(s). *BMC Biol.* **2015**, *13*, 47.
- (47) Zemel, A.; Rehfeldt, F.; Brown, A. E. X.; Discher, D. E.; Safran, S. A. Optimal matrix rigidity for stress-fibre polarization in stem cells. *Nat. Phys.* **2010**, *6*, 468–473.
- (48) Zemel, A.; Rehfeldt, F.; Brown, A. E. X.; Discher, D. E.; Safran, S. A. Cell shape, spreading symmetry, and the polarization of stress-fibers in cells. *J. Phys.: Condens. Matter* **2010**, *22*, 194110.
- (49) Rehfeldt, F.; Brown, A. E. X.; Raab, M.; Cai, S.; Zajac, A. L.; Zemel, A.; Discher, D. E. Hyaluronic acid matrices show matrix stiffness in 2D and 3D dictates cytoskeletal order and myosin-II phosphorylation within stem cells. *Integrative Biology* **2012**, *4*, 422–430.
- (50) Kanchanawong, P.; Shtengel, G.; Pasapera, A. M.; Ramko, E. B.; Davidson, M. W.; Hess, H. F.; Waterman, C. M. Nanoscale architecture of integrin-based cell adhesions. *Nature* **2010**, *468*, 580–584.
- (51) Chizhik, A. I.; Gregor, I.; Ernst, B.; Enderlein, J. Nanocavity-Based Determination of Absolute Values of Photoluminescence Quantum Yields. *ChemPhysChem* **2013**, *14* (3), 505–513.
- (52) Schneider, F.; Ruhlandt, D.; Gregor, I.; Enderlein, J.; Chizhik, A. I. Quantum yield measurements of fluorophores in lipid bilayers using a plasmonic nanocavity. *J. Phys. Chem. Lett.* **2017**, *8* (7), 1472–1475.
- (53) Grandy, C.; Port, F.; Pfeil, J.; Gottschalk, K.-E. Influence of ROCK pathway manipulation on the actin cytoskeleton height. *Cells* **2022**, *11*, 430.
- (54) Park, Y.; Depeursinge, C.; Popescu, G. Quantitative phase imaging in biomedicine. *Nat. Photonics* **2018**, *12*, 578–589.
- (55) Kaliman, S.; Jayachandran, C.; Rehfeldt, F.; Smith, A.-S. Novel growth regime of MDCK II model tissues on soft substrates. *Biophys. J.* **2014**, *106*, L25–L28.
- (56) Isbaner, S.; Karedla, N.; Ruhlandt, D.; Stein, S. C.; Chizhik, A.; Gregor, I.; Enderlein, J. Dead-time correction of fluorescence lifetime measurements and fluorescence lifetime imaging. *Opt. Express* **2016**, *24*, 9429–9445.
- (57) Chance, R.; Prock, A.; Silbey, R. Molecular fluorescence and energy transfer near interfaces. *Adv. Chem. Phys.* **2007**, *37*, 65.
- (58) Enderlein, J. A theoretical investigation of single-molecule fluorescence detection on thin metallic layers. *Biophys. J.* **2000**, *78*, 2151–2158.
- (59) Rakić, A. D.; Djurišić, A. B.; Elazar, J. M.; Majewski, M. L. Optical properties of metallic films for vertical-cavity optoelectronic devices. *Appl. Opt.* **1998**, *37*, 5271.

Recommended by ACS

Accurate Visualization of Metabolic Aberrations in Cancer Cells by Temperature Mapping with Quantum Coherence Modulation Microscopy

Haitao Zhou, Sijin Li, et al.

APRIL 27, 2023
ACS NANO

READ 

3D Chemical Imaging by Fluorescence-detected Mid-Infrared Photothermal Fourier Light Field Microscopy

Danchen Jia, Ji-Xin Cheng, et al.

MARCH 19, 2023
CHEMICAL & BIOMEDICAL IMAGING

READ 

Fluorescently Guided Optical Photothermal Infrared Microspectroscopy for Protein-Specific Bioimaging at Subcellular Level

Craig Prater, Oxana Klementieva, et al.

JANUARY 04, 2023
JOURNAL OF MEDICINAL CHEMISTRY

READ 

Specially Resolved Single Living Cell Perfusion and Targeted Fluorescence Labeling Based on Nanopipettes

Jian Lv, Ruo-Can Qian, et al.

SEPTEMBER 26, 2022
ANALYTICAL CHEMISTRY

READ 

Get More Suggestions >